





Robust Double Spatial Regularization Sparse Hyperspectral Unmixing

Fan Li , Shaoquan Zhang , *Member, IEEE*, Chengzhi Deng, Bingkun Liang , Jingjing Cao, and Shengqian Wang 

Abstract—With the help of endmember spectral library, sparse unmixing techniques have been successfully applied to hyperspectral image interpretation. The inclusion of spatial information in the sparse unmixing significantly improves the resulting fractional abundances. However, most existing spatial sparse unmixing algorithms are sensitive to noise and produce unstable solutions. To alleviate this drawback, a new robust double spatial regularization sparse unmixing (RDSRSU) method is proposed, which simultaneously exploits the spatial structure information from hyperspectral images and estimated abundance maps to mitigate the negative influence of noise on unmixing, so as to achieve robust sparse unmixing. To this end, a precalculated spatial weighting factor is introduced to maintain the original spatial information of the hyperspectral image. Meanwhile, the total variation spatial regularizer is used to capture the piecewise smooth structure of each abundance map. The experimental results, conducted by two sets of simulated data, as well as Cuprite and Mangrove real hyperspectral data, uncover that the proposed RDSRSU algorithm can offer better antinoise ability and obtain more accurate results over those gave by other advanced sparse unmixing algorithms.

Index Terms—Double spatial regularization, hyperspectral unmixing, sparse unmixing, superpixels, total variation (TV).

I. INTRODUCTION

SPECTRAL unmixing is an important technique for hyperspectral image interpretation. Hyperspectral unmixing extracts pure spectral signatures (endmembers) and estimates their proportions (abundances) in mixed pixels [1]. Unmixing methods usually depend on the expected mixing mode. Compared to nonlinear mixture model, linear mixture model

Manuscript received October 21, 2021; revised November 23, 2021; accepted November 29, 2021. Date of publication December 2, 2021; date of current version December 16, 2021. This work was supported in part by the National Natural Science Foundation of China under Grant 61901208 and Grant 61865012, in part by the China Postdoctoral Science Foundation under Grant 2020M672483, in part by the Basic Science and Technology Research Project of National Key Laboratory of Science and Technology on Automatic Target Recognition under Grant WZC20205500204, in part by the Jiangxi Provincial Key Research and Development Program under Grant 20202BBGL73081 and Grant 20181ACG70022. (*Corresponding authors: Shaoquan Zhang; Shengqian Wang.*)

Fan Li, Shaoquan Zhang, Chengzhi Deng, and Shengqian Wang are with the Jiangxi Province Key Laboratory of Water Information Cooperative Sensing and Intelligent Processing, School of Information Engineering, Nanchang Institute of Technology, Nanchang 330099, China (e-mail: lifan@nit.edu.cn; zhangshaoquan1@163.com; dengcz@nit.edu.cn; sqwang113@263.net).

Bingkun Liang and Jingjing Cao are with the Guangdong Provincial Key Laboratory of Urbanization and Geo-simulation, School of Geography and Planning, Sun Yat-sen University, Guangzhou 510275, China (e-mail: liangbk@mail2.sysu.edu.cn; caojj5@mail.sysu.edu.cn).

Digital Object Identifier 10.1109/JSTARS.2021.3132164

(LMM) has computational tractability and flexibility [2]. Many hyperspectral unmixing methods based on LMM have been proposed, including the longstanding geometry-based [3]–[7] and statistics-based [8], [9] unmixing methods. These two classes of unmixing techniques directly extract or generate endmembers from hyperspectral images, where the former relies on the pure pixels for each material present in the given scene, and the latter may produce artificial endmembers not associated with true materials.

Sparse unmixing, as a semisupervised linear spectral unmixing method, is proposed to address these issues [10]. It assumes that the pure spectral signatures of materials in mixed pixels are in a known library, and then transforms the unmixing problem into finding the optimal linear combination of component spectra that can model the hyperspectral image in the spectral library. In fact, there are only a few materials present in a mixed pixel, which is much smaller than the size of the spectral library, resulting in a sparse abundance vector [11], [12]. Some sparse unmixing algorithms focus on exploring sparse characteristics from the spectral perspective. For instance, the ℓ_1 often acts as a regularizer to yield sparse estimated abundances. Furthermore, the $\ell_{2,1}$ [13] regularizer imposes collaborative sparsity on abundance vectors, and ℓ_p (for $0 < p < 1$) [14] regularizer strengthens the sparse-inducing of fractional abundances in the procedure of unmixing. In addition, the reweighted sparse unmixing technology further enhances the sparsity of abundance solutions in various weighting ways [15], [16], such as double reweighted sparse unmixing (DRSU) [17]. On the whole, these sparse regression based hyperspectral unmixing methods have obtained promising results.

Previous works have confirmed that integrating the rich spatial information of hyperspectral images into the classic sparse unmixing formulation can guide the abundance estimation more accurately [18]. The famous total variation (TV) is included in the sparse unmixing model as a regularization term on account of spatial homogeneity among adjacent pixels, such as sparse unmixing via variable splitting augmented Lagrangian and total variation (SUnSAL-TV) [19] and DRSU-TV [20]. Nonlocal sparse unmixing [21] exploits all possible spatial information provided by similar structure in the entire image through the nonlocal means method. In [22], a constraint related to abundance estimation error is incorporated into the collaborative sparse model to reduce the influence of noise on the unmixing result. In [23], the local spectral similarity preserving regularizer is created to obtain the similarity of abundance vectors in a local

spatial area. In [24]–[29], superpixel segmentation technology is utilized to obtain the spatial region with adaptive changes in shape and size. Spectral spatial weighted sparse unmixing (S^2 WSU) [30] introduces the spectral-spatial weighting factor into the ℓ_1 regularizer sparse unmixing framework to exploit both spatial and spectral information contained in hyperspectral images. Due to the inclusion of spatial information, these algorithms alleviate the negative impact of noise to a certain extent, and have achieved favourable results. However, when the hyperspectral image is interfered by high noise, these spatially regularized unmixing methods have limited improvement in accuracy, and the estimated abundance is usually inaccurate and variable, resulting in insufficient stability of the algorithm.

In this article, a new robust double spatial regularization sparse unmixing (RDSRSU) is proposed to address the aforementioned issues. The proposed RDSRSU method consists of two parts. For the first part, the simple linear iterative clustering (SLIC) [31]–[33] algorithm is employed to segment the hyperspectral image into many homogeneous superpixel blocks, whose shape and size are adaptive. For each superpixel block, all the elements in it are averaged, and the obtained average value is assigned to all the elements as a new value. That is, each element in a superpixel set has the same value. Based on this, we obtain a reconstructed coarse hyperspectral image. Subsequently, the reconstructed image is unmixed by solving the sparse constrained optimization problem, thus, the corresponding coarse abundance map is estimated. Then, a spatial weight is constructed based on the coarse abundance map, each entry of which is inversely proportional to the ℓ_2 norm of a row vector in the abundance matrix. The spatial weight is designed to promote the spatial correlation between pixels and the rowwise sparsity of abundance solutions. For the second part, the nonisotropic TV regularization is introduced to promote piecewise transitions in estimated abundances among adjacent pixels. The main contributions of this article are summarized as follows.

- 1) A new precalculated spatial weight is proposed for robust sparse hyperspectral unmixing. It is derived from the reconstructed coarse hyperspectral image, and the image reconstruction aims to alleviate the negative impact of noise via the local spatial homogeneity of the pixels in the superpixel set. Therefore, the new spatial weight can still remain the precise spatial information of the image even under high noise interference.
- 2) Another spatial regularizer, i.e., the TV term, is introduced to impose sparsity on the difference domain of the abundance map, which further promotes the neighboring spatial homogeneity and smoothness of the image. The proposed method shows apparent improvement in unmixing performance and affords the potential to enhance antinoise ability by including dual spatial constraint on top of the classic sparse regression formulation.

The rest of this article is organized as follows. Section II presents the sparse unmixing formulations and several variant sparse unmixing models. Section III describes in detail the proposed RDSRSU technique and its solution process. In Sections IV and V, we exhibit the experiment results and give

a comprehensive evaluation. Some conclusions and future research routes are drawn in Section VI.

II. BACKGROUND

A. Linear Mixture Model

Let $\mathbf{Y} = [\mathbf{y}_1, \dots, \mathbf{y}_n] \in \mathbb{R}^{d \times n}$ be the observed data, where d and n are the number of bands and pixels, respectively. Let $\mathbf{A} \in \mathbb{R}^{d \times m}$ be the known library with m spectral signatures. We assume that the spectra of all potential endmembers can be found in the spectral library \mathbf{A} , then LMM can be described as

$$\mathbf{Y} = \mathbf{A}\mathbf{X} + \mathbf{N} \text{ s.t. } \mathbf{X} \geq 0 \quad (1)$$

where $\mathbf{X} = [\mathbf{x}_1, \dots, \mathbf{x}_n] \in \mathbb{R}^{m \times n}$ is the abundance matrix, $\mathbf{N} \in \mathbb{R}^{d \times n}$ is noise and model error, and $\mathbf{X} \geq 0$ denotes the abundance nonnegativity constraint (ANC). The abundance sum-to-one constraint (ASC) of the form $\mathbf{1}^T \mathbf{x} = 1$ is not explicitly enforced herein due to the defects stated in [10].

B. Sparse Unmixing

From the physical meaning of abundance, we know that each row in the abundance matrix represents fractional abundances with regard to a substance in the spectral library, and each column represents the proportion of entries in the library in a pixel. In practical terms, there are only a few spectral signatures involved in modeling an image compared to the entries in the library, which results in the presence of many zeros in fractional abundances [34], [35]. That is, the abundance matrix is inherently sparse. Therefore, hyperspectral unmixing is transformed into a sparse linear regression problem related to abundance estimation, which is formulated as follows:

$$\min_{\mathbf{X}} \frac{1}{2} \|\mathbf{Y} - \mathbf{A}\mathbf{X}\|_F^2 + \lambda \|\mathbf{X}\|_0 \text{ s.t. } \mathbf{X} \geq 0 \quad (2)$$

where $\|\cdot\|_F$ is the Frobenius norm, $\|\mathbf{X}\|_0$ counts the nonzero components in \mathbf{X} , and $\lambda \geq 0$ is a constant penalty parameter. The optimization problem (2) is NP-hard. SUnSAL [10] takes a convex relaxed strategy for computing problem (2), which replaces the ℓ_0 norm with the ℓ_1 norm, and obtains the convex optimization problem as follows:

$$\min_{\mathbf{X}} \frac{1}{2} \|\mathbf{Y} - \mathbf{A}\mathbf{X}\|_F^2 + \lambda \|\mathbf{X}\|_{1,1} \text{ s.t. } \mathbf{X} \geq 0 \quad (3)$$

where $\|\mathbf{X}\|_{1,1} = \sum_{j=1}^n \|\mathbf{x}_j\|_1$, \mathbf{x}_j is the j th column vector of \mathbf{X} . The ℓ_1 norm regularization essentially imposes sparsity on each abundance vector in an independent manner, rather than considering the correlation between each pixel and its neighbors.

Taking account of the spatial-contextual information, SUnSAL-TV incorporates the nonisotropic TV regularizer into the aforementioned classic sparse unmixing formulation. The SUnSAL-TV optimization problem is, thus,

$$\min_{\mathbf{X}} \frac{1}{2} \|\mathbf{Y} - \mathbf{A}\mathbf{X}\|_F^2 + \lambda \|\mathbf{X}\|_{1,1} + \lambda_{\text{TV}} \text{TV}(\mathbf{X}) \text{ s.t. } \mathbf{X} \geq 0 \quad (4)$$

where $\text{TV}(\mathbf{X}) \equiv \sum_{p,q \in \mathcal{N}} \|\mathbf{x}_p - \mathbf{x}_q\|_1$, \mathcal{N} is the set of horizontal and vertical neighboring pixels in the image, and $\lambda_{\text{TV}} \geq 0$ is

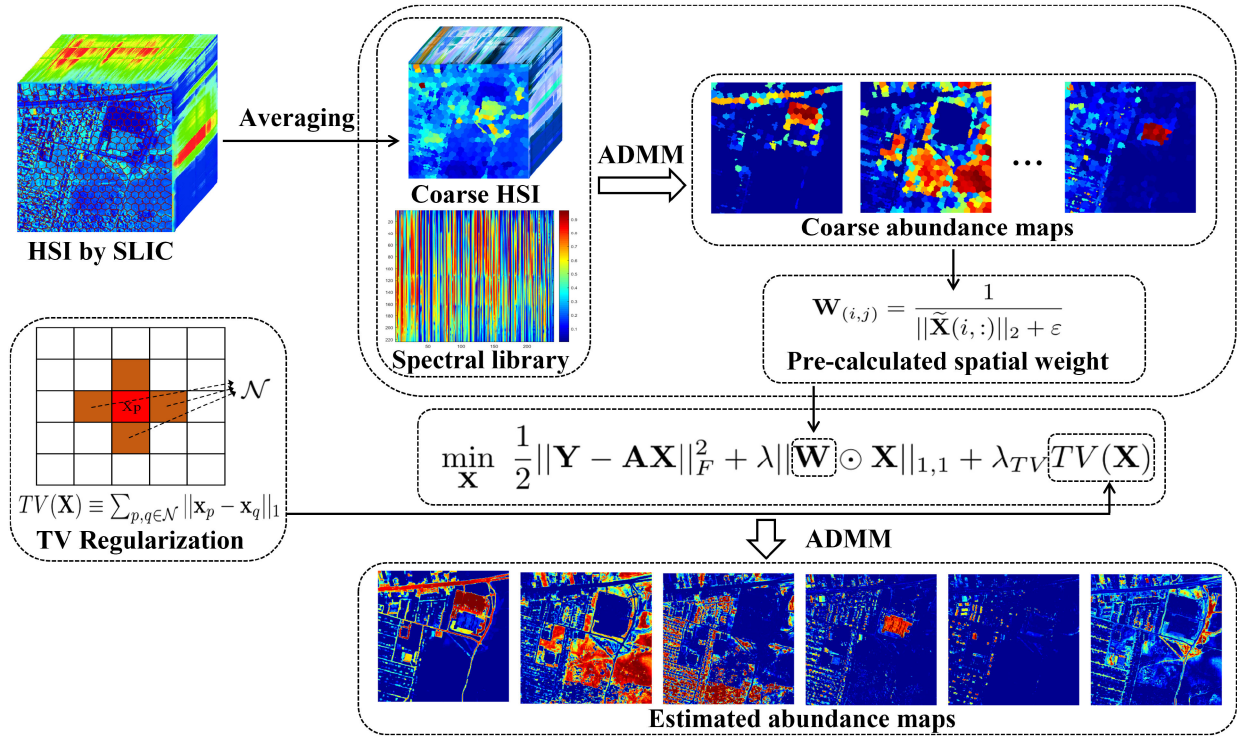


Fig. 1. Flowchart of the proposed RDSRSU method (HSI means hyperspectral image).

a regularization parameter. The minimization of TV term promotes piecewise smooth transitions in the abundance map of the same endmember among neighboring pixels [19].

III. PROPOSED ROBUST DOUBLE SPATIAL REGULARIZATION SPARSE UNMIXING ALGORITHM

A. Formulation of Proposed RDSRSU Model

Previous studies have shown that the integration of spatial information, whether in unmixing procedure itself or as a preprocessing step, contributes to improving the accuracy of the abundance estimation [36], [37]. The weighting factor related to the spatial location is introduced into the spectral unmixing model, which is a simple way to exploit spatial information [30]. In addition to the spatial proximity, the similarity of abundance vectors is another effective way to explore the spatial correlation of pixels [38], [39]. Nonetheless, most existing spatial regularization strategies are designed on estimated abundances. When hyperspectral data is seriously contaminated by noise, it is difficult to accurately estimate abundances by only relying on the abundance itself to be updated iteratively during the unmixing process. Even if spatial regularization is implemented, estimated abundances with large deviations are still hard to correct, resulting in inaccurate and unstable solutions. In other words, such algorithms are vulnerable to noise.

In order to improve the noise robustness of the unmixing algorithm, a new spatial weight is built on the noise reduction preprocessing hyperspectral image, as an alternative to the traditional weight merely built on the estimated abundance, to guide the abundance estimation. More specifically, a coarse

hyperspectral image is reconstructed by virtue of the similarity of pixels in the origin hyperspectral image in both location and spectrum, which is similar to the mean filter and plays a role in image denoising. Subsequently, the coarse-scale weight guide matrix is predictively established based on the reconstructed hyperspectral image. Since the weight guide matrix is obtained from an approximate denoised image, it is robust to noise. Then, the new spatial weight is rowwise calculated from the weight guide matrix, and the precalculated spatial weight is introduced into the ℓ_1 regularizer in the unmixing model to induce the estimated abundance to converge toward the preidentified endmember rows. It should be noted that the new spatial weight is also insensitive to noise. Combining the traditional TV regularizer to impose sparsity on the difference domain of the abundance map, a RDSRSU method is proposed.

The flowchart of RDSRSU method is shown in Fig. 1. First of all, a coarse hyperspectral image is constructed, which is derived from the superpixel segmentation of the original hyperspectral image. Suppose that $\mathbf{Y} \in \mathbb{R}^{d \times n}$ is the original hyperspectral image, and it is divided into s superpixel blocks by the SLIC algorithm [31], [33]; $\mathbf{Y}_t \in \mathbb{R}^{d \times n_t}$ ($t = 1, \dots, s, \sum_{t=1}^s n_t = n$) is the t th superpixel block, containing n_t pixels, and $\mathbf{y}_k \in \mathbb{R}^{d \times 1}$ ($k = 1, \dots, n_t$) is any pixel (column) in \mathbf{Y}_t . With these assumptions in place, the coarse image $\tilde{\mathbf{Y}} \in \mathbb{R}^{d \times n}$ is reconstructed as follows:

$$\tilde{\mathbf{y}}_k = \frac{1}{n_t} \sum_{k=1}^{n_t} \mathbf{y}_k \quad (5)$$

where $\tilde{\mathbf{y}}_k$ represents any column in the coarse pixel $\tilde{\mathbf{Y}}_t$ corresponding to the superpixel block \mathbf{Y}_t . It should be noted that the columns in the same coarse pixel have the same values, and the superpixel blocks in the original image are mapped to the coarse pixels in the reconstructed image one by one.

Subsequently, the weight guide matrix $\tilde{\mathbf{X}}$ can be obtained by using alternating direction method of multipliers (ADMM) [40] to unmix the coarse hyperspectral image. For simplicity, we solve the following optimization problem:

$$\arg \min_{\tilde{\mathbf{X}}} \frac{1}{2} \|\tilde{\mathbf{Y}} - \mathbf{A}\tilde{\mathbf{X}}\|_F^2 + \lambda \|\tilde{\mathbf{X}}\|_{1,1} \quad \text{s.t. } \tilde{\mathbf{X}} \geq 0. \quad (6)$$

The coarse hyperspectral image averages all the elements in each homogeneous region, which alleviates the impact of noise effectively, so the resulting weight guide matrix is insensitive to noise.

Furthermore, considering the rowwise sparsity of the abundance matrix, the spatial weight \mathbf{W} is constructed as follows:

$$\mathbf{W}_{(i,j)} = \frac{1}{\|\tilde{\mathbf{X}}(i, :)\|_2 + \varepsilon}, \quad i = 1, \dots, m, \quad j = 1, \dots, n \quad (7)$$

where $\mathbf{W}_{(i,j)}$ is the element in the i th row and j th column of \mathbf{W} , $\tilde{\mathbf{X}}(i, :)$ is the i th row vector of $\tilde{\mathbf{X}}$, and $\varepsilon > 0$ is an additional small constant to avoid singularities. Each entry of \mathbf{W} is inversely proportional to the ℓ_2 norm of a row in the weight guide matrix.

The constructed spatial weight is introduced as a priori into the model (4), and the RDSRSU model is proposed

$$\begin{aligned} \min_{\mathbf{X}} \quad & \frac{1}{2} \|\mathbf{Y} - \mathbf{A}\mathbf{X}\|_F^2 + \lambda \|\mathbf{W} \odot \mathbf{X}\|_{1,1} + \lambda_{\text{TV}} \text{TV}(\mathbf{X}) \\ \text{s.t. } \quad & \mathbf{X} \geq 0 \end{aligned} \quad (8)$$

where \odot denotes the Hadamard product of two variables.

The precalculated spatial weight is obtained from the reconstructed coarse pixel image based on superpixel, which implies the spatial and spectral information of the image. Moreover, the spatial weight enables estimated abundances to concentrate on a few lines, resulting in the rowwise sparse abundance matrix. The nonisotropic TV regularizer imposes spatial consistency on estimated abundances. The spatial weight focuses on pixels in homogeneous regions of the image, while the TV term focused on the relationship of the abundance vectors among adjacent pixels. The dual spatial constraints provide the potential to enhance antinoise ability and improve unmixing performance.

B. Optimization by the ADMM

We solve the optimization problem related to the proposed RDSRSU model by ADMM. Define

$$\mathbf{H}\mathbf{X} \equiv \begin{bmatrix} \mathbf{H}_h \mathbf{X} \\ \mathbf{H}_v \mathbf{X} \end{bmatrix}$$

where \mathbf{H}_h and \mathbf{H}_v denote two linear operators that, respectively, calculate the differences between the horizontal and vertical neighboring pixels of \mathbf{X} . Then, the optimization problem (8)

can be rewritten as

$$\begin{aligned} \min_{\mathbf{X}} \quad & \frac{1}{2} \|\mathbf{Y} - \mathbf{A}\mathbf{X}\|_F^2 + \lambda \|\mathbf{W} \odot \mathbf{X}\|_{1,1} + \\ & \lambda_{\text{TV}} \|\mathbf{H}\mathbf{X}\|_{1,1} + \iota_{R^+}(\mathbf{X}) \quad \text{s.t. } \mathbf{X} \geq 0 \end{aligned} \quad (9)$$

where $\iota_{R^+}(\mathbf{X}) = \sum_{j=1}^n \iota_{R^+}(\mathbf{x}_j)$ is the indicator function, i.e., $\iota_{R^+}(\mathbf{x}_j)$ is zero if \mathbf{x}_j is non-negative and $+\infty$ otherwise.

In order to split the original optimization problem into several subproblems, auxiliary matrices \mathbf{U} , \mathbf{V}_1 , \mathbf{V}_2 , \mathbf{V}_3 , \mathbf{V}_4 , \mathbf{V}_5 are introduced, and the equivalent problem of (9) is formulated as

$$\begin{aligned} \min_{\mathbf{U}, \mathbf{V}_1, \mathbf{V}_2, \mathbf{V}_3, \mathbf{V}_4, \mathbf{V}_5} \quad & \frac{1}{2} \|\mathbf{Y} - \mathbf{V}_1\|_F^2 + \lambda \|\mathbf{W} \odot \mathbf{V}_2\|_{1,1} \\ & + \lambda_{\text{TV}} \|\mathbf{V}_4\|_{1,1} + \iota_{R^+}(\mathbf{V}_5) \\ \text{s.t. } \quad & \mathbf{V}_1 = \mathbf{A}\mathbf{U}, \mathbf{V}_2 = \mathbf{U}, \mathbf{V}_3 = \mathbf{U}, \mathbf{V}_4 = \mathbf{H}\mathbf{V}_3, \mathbf{V}_5 = \mathbf{U}. \end{aligned} \quad (10)$$

A compact form of problem (10) is

$$\min_{\mathbf{U}, \mathbf{V}} g(\mathbf{U}, \mathbf{V}) \quad \text{s.t. } \mathbf{G}\mathbf{U} + \mathbf{B}\mathbf{V} = \mathbf{0} \quad (11)$$

where $\mathbf{V} \equiv (\mathbf{V}_1, \mathbf{V}_2, \mathbf{V}_3, \mathbf{V}_4, \mathbf{V}_5)^T$, $g(\mathbf{U}, \mathbf{V}) \equiv \frac{1}{2} \|\mathbf{Y} - \mathbf{V}_1\|_F^2 + \lambda \|\mathbf{W} \odot \mathbf{V}_2\|_{1,1} + \lambda_{\text{TV}} \|\mathbf{V}_4\|_{1,1} + \iota_{R^+}(\mathbf{V}_5)$, $\mathbf{G} = (\mathbf{A}, \mathbf{I}, \mathbf{I}, \mathbf{0}, \mathbf{I})^T$, and

$$\mathbf{B} = \begin{bmatrix} -\mathbf{I} & \mathbf{0} & \mathbf{0} & \mathbf{0} & \mathbf{0} \\ \mathbf{0} & -\mathbf{I} & \mathbf{0} & \mathbf{0} & \mathbf{0} \\ \mathbf{0} & \mathbf{0} & -\mathbf{I} & \mathbf{0} & \mathbf{0} \\ \mathbf{0} & \mathbf{0} & \mathbf{H} & -\mathbf{I} & \mathbf{0} \\ \mathbf{0} & \mathbf{0} & \mathbf{0} & \mathbf{0} & -\mathbf{I} \end{bmatrix}.$$

The augmented Lagrangian for optimization problem (11) is

$$\mathcal{L}(\mathbf{U}, \mathbf{V}, \mathbf{D}) = g(\mathbf{U}, \mathbf{V}) + \frac{\mu}{2} \|\mathbf{G}\mathbf{U} + \mathbf{B}\mathbf{V} - \mathbf{D}\|_F^2 \quad (12)$$

where $\mu > 0$ is a penalty parameter, and $\mathbf{D} = \{\mathbf{D}_1, \mathbf{D}_2, \mathbf{D}_3, \mathbf{D}_4, \mathbf{D}_5\}$ is the Lagrangian multipliers. $\mathcal{L}(\mathbf{U}, \mathbf{V}, \mathbf{D})$ is iteratively optimized for \mathbf{U} and \mathbf{V} under the framework of ADMM. In each iteration, following subproblems are solved sequentially.

The optimization subproblem with regards to \mathbf{U} is

$$\begin{aligned} \mathbf{U}^{(k+1)} \leftarrow \arg \min_{\mathbf{U}} \quad & \frac{\mu}{2} \|\mathbf{A}\mathbf{U} - \mathbf{V}_1^{(k)} - \mathbf{D}_1^{(k)}\|_F^2 \\ & + \frac{\mu}{2} \|\mathbf{U} - \mathbf{V}_2^{(k)} - \mathbf{D}_2^{(k)}\|_F^2 \\ & + \frac{\mu}{2} \|\mathbf{U} - \mathbf{V}_3^{(k)} - \mathbf{D}_3^{(k)}\|_F^2 \\ & + \frac{\mu}{2} \|\mathbf{U} - \mathbf{V}_5^{(k)} - \mathbf{D}_5^{(k)}\|_F^2. \end{aligned} \quad (13)$$

\mathbf{U} is obtained by taking the partial derivative of \mathbf{U} in problem (13), and the solution is

$$\begin{aligned} \mathbf{U}^{(k+1)} \leftarrow (\mathbf{A}^T \mathbf{A} + 3\mathbf{I})^{-1} (\mathbf{A}^T (\mathbf{V}_1^{(k)} + \mathbf{D}_1^{(k)}) \\ + (\mathbf{V}_2^{(k)} + \mathbf{D}_2^{(k)}) + (\mathbf{V}_3^{(k)} + \mathbf{D}_3^{(k)}) \\ + (\mathbf{V}_5^{(k)} + \mathbf{D}_5^{(k)})). \end{aligned} \quad (14)$$

The \mathbf{V} subproblem is decoupled into five subparts. Calculate \mathbf{V}_1 as

$$\begin{aligned} \mathbf{V}_1^{(k+1)} \leftarrow \arg \min_{\mathbf{V}_1} & \frac{1}{2} \|\mathbf{Y} - \mathbf{V}_1\|_F^2 \\ & + \frac{\mu}{2} \|\mathbf{A}\mathbf{U}^{(k+1)} - \mathbf{V}_1 - \mathbf{D}_1^{(k)}\|_F^2. \end{aligned} \quad (15)$$

Solve problem (15) in the same way as problem (13), and get

$$\mathbf{V}_1^{(k+1)} \leftarrow \frac{1}{1+\mu} [\mathbf{Y} + \mu(\mathbf{A}\mathbf{U}^{(k+1)} - \mathbf{D}_1^{(k)})]. \quad (16)$$

\mathbf{V}_2 is calculated as follows:

$$\begin{aligned} \mathbf{V}_2^{(k+1)} \leftarrow \arg \min_{\mathbf{V}_2} & \lambda \|\mathbf{W} \odot \mathbf{V}_2\|_{1,1} \\ & + \frac{\mu}{2} \|\mathbf{U}^{(k+1)} - \mathbf{V}_2 - \mathbf{D}_2^{(k)}\|_F^2. \end{aligned} \quad (17)$$

The solution to \mathbf{V}_2 is obtained

$$\mathbf{V}_2^{(k+1)} \leftarrow \text{soft}(\mathbf{U}^{(k+1)} - \mathbf{D}_2^{(k)}, \frac{\lambda}{\mu} \mathbf{W}) \quad (18)$$

where $\text{soft}(\cdot, \tau)$ denotes the soft-threshold function $y \mapsto \text{sign}(y) \max\{|y| - \tau, 0\}$.

Calculate \mathbf{V}_3 via the following problem:

$$\begin{aligned} \mathbf{V}_3^{(k+1)} \leftarrow \arg \min_{\mathbf{V}_3} & \frac{\mu}{2} \|\mathbf{U}^{(k+1)} - \mathbf{V}_3 - \mathbf{D}_3^{(k)}\|_F^2 \\ & + \frac{\mu}{2} \|\mathbf{H}\mathbf{V}_3 - \mathbf{V}_4^{(k)} - \mathbf{D}_4^{(k)}\|_F^2. \end{aligned} \quad (19)$$

The solution to (19) is

$$\begin{aligned} \mathbf{V}_3^{(k+1)} \leftarrow & (\mathbf{H}^T \mathbf{H} + \mathbf{I})^{-1} (\mathbf{U}^{(k+1)} - \mathbf{D}_3^{(k)} \\ & + \mathbf{H}^T \mathbf{V}_4^{(k)} + \mathbf{H}^T \mathbf{D}_4^{(k)}). \end{aligned} \quad (20)$$

The subproblem for \mathbf{V}_4 is

$$\mathbf{V}_4^{(k+1)} \leftarrow \arg \min_{\mathbf{V}_4} \lambda_{TV} \|\mathbf{V}_4\|_{1,1} + \frac{\mu}{2} \|\mathbf{H}\mathbf{V}_3^{(k)} - \mathbf{V}_4 - \mathbf{D}_4^{(k)}\|_F^2. \quad (21)$$

The solution to (21) is the soft threshold

$$\mathbf{V}_4^{(k+1)} \leftarrow \text{soft}(\mathbf{H}\mathbf{V}_3^{(k+1)} - \mathbf{D}_4^{(k)}, \frac{\lambda_{TV}}{\mu}). \quad (22)$$

The subproblem for \mathbf{V}_5 is

$$\mathbf{V}_5^{(k+1)} \leftarrow \arg \min_{\mathbf{V}_5} \iota_{R^+}(\mathbf{V}_5) + \frac{\mu}{2} \|\mathbf{U}^{(k+1)} - \mathbf{V}_5 - \mathbf{D}_5^{(k)}\|_F^2. \quad (23)$$

The solution to \mathbf{V}_5 is

$$\mathbf{V}_5^{(k+1)} \leftarrow \max(\mathbf{U}^{(k+1)} - \mathbf{D}_5^{(k)}, 0). \quad (24)$$

And finally, we update the Lagrange multipliers as follows:

$$\mathbf{D}^{(k+1)} = \mathbf{D}^{(k)} - (\mathbf{G}\mathbf{U}^{(k+1)} + \mathbf{B}\mathbf{V}^{(k+1)}). \quad (25)$$

For clarity, we summarize the proposed RDSRSU algorithm and show its pseudocode in the Algorithm 1.

The RDSRSU algorithm iteratively updates the auxiliary variables and Lagrange multipliers in the ADMM framework, and its convergence is difficult to prove. Fig. 2 shows the residual

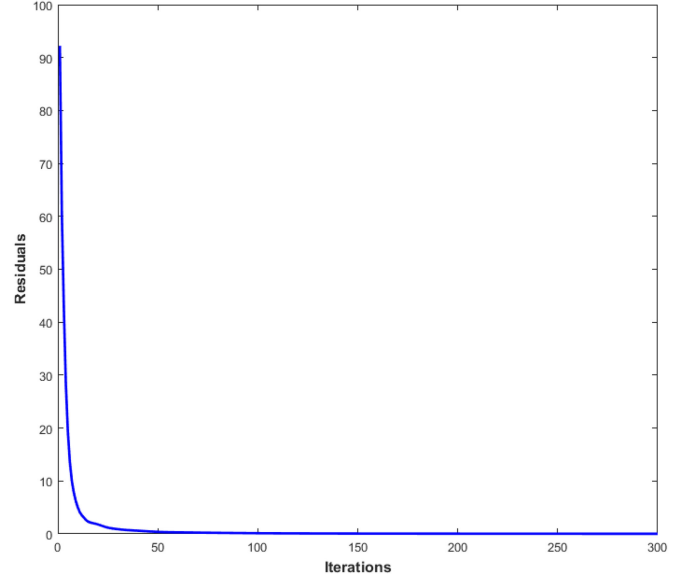


Fig. 2. Residual $\|\mathbf{G}\mathbf{U}^{(t)} + \mathbf{B}\mathbf{V}^{(t)}\|_F$ as a function of iteration times for the proposed algorithm.

Algorithm 1: Pseudocode of the RDSRSU Algorithm.

Step 1:

- 1: **Input:**
- 2: \mathbf{Y} , \mathbf{A} , SLIC parameters
- 3: Perform superpixel segmentation on \mathbf{Y} by SLIC algorithm
- 4: Calculate (5) to reconstruct the coarse image $\tilde{\mathbf{Y}}$
- 5: Solve the optimization problem (6) by SUnSAL algorithm
- 6: Calculate (7) to obtain the spatial weight \mathbf{W}

Step 2:

1: Initialization:

- 2: set $k = 0$, choose

$$\mu, \lambda, \lambda_{TV}, \varepsilon > 0, \mathbf{U}^{(0)}, \mathbf{V}_1^{(0)}, \dots, \mathbf{V}_5^{(0)}, \mathbf{D}_1^{(0)}, \dots, \mathbf{D}_5^{(0)}$$

3: Update iteration:

- 4: $\mathbf{U}^{(k+1)} \leftarrow (\mathbf{A}^T \mathbf{A} + 3\mathbf{I})^{-1} (\mathbf{A}^T (\mathbf{V}_1^{(k)} + \mathbf{D}_1^{(k)}) + (\mathbf{V}_2^{(k)} + \mathbf{D}_2^{(k)}) + (\mathbf{V}_3^{(k)} + \mathbf{D}_3^{(k)}) + (\mathbf{V}_5^{(k)} + \mathbf{D}_5^{(k)}))$
 - 5: $\mathbf{V}_1^{(k+1)} \leftarrow \frac{1}{1+\mu} [\mathbf{Y} + \mu(\mathbf{A}\mathbf{U}^{(k+1)} - \mathbf{D}_1^{(k)})]$
 - 6: $\mathbf{V}_2^{(k+1)} \leftarrow \text{soft}(\mathbf{U}^{(k+1)} - \mathbf{D}_2^{(k)}, \frac{\lambda}{\mu} \mathbf{W})$
 - 7: $\mathbf{V}_3^{(k+1)} \leftarrow (\mathbf{H}^T \mathbf{H} + \mathbf{I})^{-1} (\mathbf{U}^{(k+1)} - \mathbf{D}_3^{(k)} + \mathbf{H}^T \mathbf{V}_4^{(k)} + \mathbf{H}^T \mathbf{D}_4^{(k)})$
 - 8: $\mathbf{V}_4^{(k+1)} \leftarrow \text{soft}(\mathbf{H}\mathbf{V}_3^{(k+1)} - \mathbf{D}_4^{(k)}, \frac{\lambda_{TV}}{\mu})$
 - 9: $\mathbf{V}_5^{(k+1)} \leftarrow \max(\mathbf{U}^{(k+1)} - \mathbf{D}_5^{(k)}, 0)$
 - 10: $\mathbf{D}_1^{(k+1)} \leftarrow \mathbf{D}_1^{(k)} - \mathbf{A}\mathbf{U}^{(k+1)} + \mathbf{V}_1^{(k+1)}$
 - 11: $\mathbf{D}_2^{(k+1)} \leftarrow \mathbf{D}_2^{(k)} - \mathbf{U}^{(k+1)} + \mathbf{V}_2^{(k+1)}$
 - 12: $\mathbf{D}_3^{(k+1)} \leftarrow \mathbf{D}_3^{(k)} - \mathbf{U}^{(k+1)} + \mathbf{V}_3^{(k+1)}$
 - 13: $\mathbf{D}_4^{(k+1)} \leftarrow \mathbf{D}_4^{(k)} - \mathbf{H}\mathbf{V}_3^{(k+1)} + \mathbf{V}_4^{(k+1)}$
 - 14: $\mathbf{D}_5^{(k+1)} \leftarrow \mathbf{D}_5^{(k)} - \mathbf{U}^{(k+1)} + \mathbf{V}_5^{(k+1)}$
 - 15: **Update iteration:** $k \leftarrow k + 1$
 - 16: **until** some stopping criterion is satisfied.
-

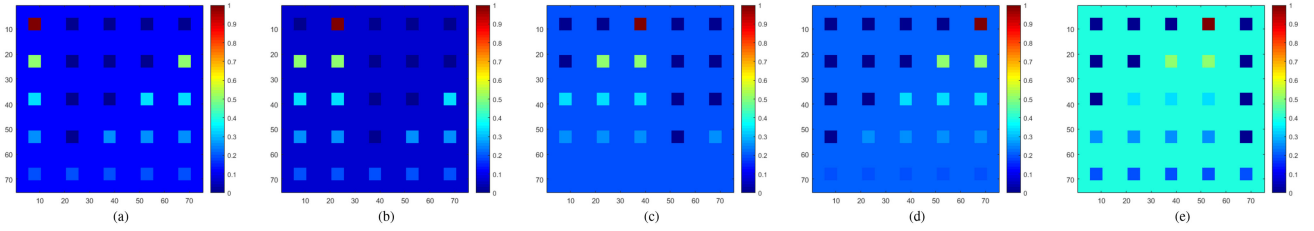


Fig. 3. Actual fractional abundance of endmembers in DC1 simulated data. (a) Endmember 1. (b) Endmember 2. (c) Endmember 3. (d) Endmember 4. (e) Endmember 5.

$\|\mathbf{GU}^{(t)} + \mathbf{BV}^{(t)}\|_F$ as a function of iteration times for the proposed algorithm. As shown in Fig. 2, the residual reaches a stable level close to zero when the number of iterations arrives at 50. Therefore, the maximum iteration times is set to 300 in our experiments, which guarantees the convergence of the proposed algorithm. Furthermore, when the residual meets the error tolerance (a small positive constant, such as $1e-5$), it can be inferred that the algorithm has converged and the proposed algorithm can be stopped.

IV. EXPERIMENTS WITH SYNTHETIC DATA

In this section, we demonstrate the effectiveness of the proposed RDSRSU algorithm on two synthetic hyperspectral datasets. The proposed RDSRSU algorithm will be compared with five effective sparse unmixing algorithms, including SUNSAL [10], SUNSAL-TV [19], DRSU [17], DRSU-TV [20], and S^2 WSU [30] algorithms. It should be noted that SUNSAL and DRSU are two classical spectral-based algorithms, SUNSAL-TV and DRSU-TV are two representative algorithms that take into account TV regularization, and S^2 WSU is an advanced unmixing algorithm that includes a weighted sparse regularizer. The signal-to-reconstruction error (SRE, measured in dB) is adopted to evaluate the quality of unmixing results quantitatively. The SRE (dB) is defined as

$$\text{SRE}(\text{dB}) = 10 \cdot \log_{10}(E(\|\mathbf{x}\|_2^2)/E(\|\mathbf{x} - \hat{\mathbf{x}}\|_2^2)) \quad (26)$$

where \mathbf{x} and $\hat{\mathbf{x}}$ are the actual fractional abundances and estimated abundances, respectively, and $E(\cdot)$ denotes the expectation function. Furthermore, another metric, i.e., the probability of success p_s , is used to quantitatively evaluate the stability of the estimation, which is calculated as: $p_s \equiv P(\|\hat{\mathbf{x}} - \mathbf{x}\|^2/\|\mathbf{x}\|^2 \leq \text{threshold})$. In [10], the result is deemed successful when $\|\hat{\mathbf{x}} - \mathbf{x}\|^2/\|\mathbf{x}\|^2 \leq 3.16$ (5 dB). The higher the SRE (dB) or p_s , the better the unmixing performance.

A. Simulated Datasets

Two mineral spectral libraries are used in the simulated data experiment, both of which are subsets of USGS library.¹ The spectral library $\mathbf{A}_1 \in \mathbb{R}^{224 \times 240}$ contains 240 endmembers randomly chosen from USGS library and 224 bands uniformly covering the wavelength range from 0.4 to 2.5 μm . The spectral library $\mathbf{A}_2 \in \mathbb{R}^{221 \times 222}$ consists of 222 endmembers with 221 bands. Two simulated data cubes were generated using particular

fractional abundances that satisfy the ANC and ASC, which are described in detail as follows.

- 1) *Simulated Data Cube 1* (DC1): The size of DC1 is 75×75 pixels and each pixel has 224 bands. As described in [19], five endmembers randomly chosen from \mathbf{A}_1 participate in generating the test data. The actual abundance maps for the five endmembers are exhibited in Fig. 3. Synthetic data are subsequently corrupted by i.i.d. Gaussian noise with signal-to-noise ratios (SNR) are 10, 20, and 30 dB, respectively.
- 2) *Simulated Data Cube 2* (DC2): The size of DC2 is 128×128 pixels and each pixel has 221 bands. It is generated using MATLAB-based hyperspectral imagery synthesis toolbox released by the Computational Intelligence Group at the University of the Basque University.² Five endmembers randomly chosen from the spectral library \mathbf{A}_2 are distributed with reference to the actual abundance maps shown in Fig. 4 to simulate the data cube 2, and then the data are also contaminated by i.i.d. Gaussian noise with SNR=10, 20, and 30 dB.

B. Results and Discussion

Tables I and II, respectively, exhibit the SRE (dB) and p_s values obtained by performing different unmixing algorithm on DC1 and DC2, which cover all three SNR levels. The optimal parameter settings for each algorithm to obtain the best scores are given in parentheses. Moreover, for precalculating the spatial weight for RDSRSU, the parameter of SUNSAL (in step 5 of Algorithm 1) is set to $\lambda = 5e-3$. It is observed from Tables I and II, the proposed RDSRSU algorithm obtains higher SRE (dB) and p_s than S^2 WSU, DRSU-TV, DRSU, SUNSAL-TV, SUNSAL in all cases. In particular, even if the data are occupied by noise (SNR=10 dB), RDSRSU can perform well. Compared with other algorithms, the integration of two spatial regularization strategies into the sparse unmixing model provides the potential to enhance the accuracy of abundance estimation in two different analysis scenarios, which makes the RDSRSU algorithm show significant advantages and strong robustness. In the case of relatively low noise, the performance of DRSU and S^2 WSU algorithms has been greatly improved, since the former integrates spectral weights to promote the row sparsity

¹[Online]. Available: <http://speclab.cr.usgs.gov/spectral.lib06>

²[Online]. Available: www.ehu.es/ccwintco/index.php/Hyperspectral_Imagery_Synthesis_tools_for_MATLAB

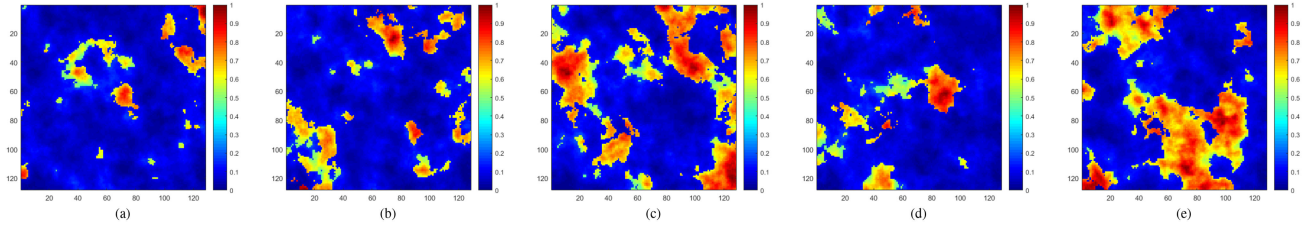


Fig. 4. Actual fractional abundance of endmembers in DC2 simulated data. (a) Endmember 1. (b) Endmember 2. (c) Endmember 3. (4) Endmember 4. (5) Endmember 5.

TABLE I
SRE (dB) AND p_s VALUES OBTAINED BY PERFORMING COMPARISON ALGORITHMS AND THE PROPOSED RDSRSU ALGORITHM ON DC1
(THE RELEVANT PARAMETERS ARE LISTED OPTIMAL IN THE PARENTHESES)

Algorithm	SUnSAL		SUnSAL-TV		DRSU		DRSU-TV		S ² WSU		RDSRSU	
	SRE(dB)	p_s	SRE(dB)	p_s	SRE(dB)	p_s	SRE(dB)	p_s	SRE(dB)	p_s	SRE(dB)	p_s
SNR=10dB	0.1380	0.0028	5.7396	0.9166	0.3453	0.0210	6.2136	0.9218	2.7553	0.2380	13.0857	0.9808
	$(\lambda = 1)$		$(\lambda = 2e-1, \lambda_{TV} = 2e-1)$		$(\lambda = 1.5)$		$(\lambda = 9e-1, \lambda_{TV} = 3e-1)$		$(\lambda = 4)$		$(\lambda = 6e-2, \lambda_{TV} = 3e-1)$	
SNR=20dB	2.9056	0.1812	7.2285	0.9641	4.6915	0.6526	7.4825	0.9586	5.1079	0.7888	20.2828	1
	$(\lambda = 5e-1)$		$(\lambda = 3e-2, \lambda_{TV} = 5e-2)$		$(\lambda = 4e-1)$		$(\lambda = 5e-4, \lambda_{TV} = 5e-2)$		$(\lambda = 2e-1)$		$(\lambda = 4e-2, \lambda_{TV} = 3e-2)$	
SNR=30dB	6.1703	0.8217	15.4700	0.9954	12.9237	0.9988	25.0311	1	16.0868	1	28.0006	1
	$(\lambda = 5e-2)$		$(\lambda = 6e-3, \lambda_{TV} = 2e-2)$		$(\lambda = 4e-3)$		$(\lambda = 3e-3, \lambda_{TV} = 7e-3)$		$(\lambda = 1e-3)$		$(\lambda = 2e-2, \lambda_{TV} = 7e-3)$	

TABLE II
SRE (dB) AND p_s VALUES OBTAINED BY PERFORMING COMPARISON ALGORITHMS AND THE PROPOSED RDSRSU ALGORITHM ON DC2
(THE RELEVANT PARAMETERS ARE LISTED OPTIMAL IN THE PARENTHESES)

Algorithm	SUnSAL		SUnSAL-TV		DRSU		DRSU-TV		S ² WSU		RDSRSU	
	SRE(dB)	p_s	SRE(dB)	p_s	SRE(dB)	p_s	SRE(dB)	p_s	SRE(dB)	p_s	SRE(dB)	p_s
SNR=10dB	2.0790	0.2944	5.4107	0.7228	0.2733	0	6.1675	0.8218	5.3775	0.7882	12.2871	0.9570
	$(\lambda = 2)$		$(\lambda = 8e-1, \lambda_{TV} = 1e-1)$		$(\lambda = 6)$		$(\lambda = 1e-1, \lambda_{TV} = 1e-1)$		$(\lambda = 7e-1)$		$(\lambda = 2e-1, \lambda_{TV} = 1e-1)$	
SNR=20dB	5.6219	0.7560	10.1667	0.9164	9.7377	0.9453	15.9078	0.9906	12.7466	0.9841	18.9668	0.9969
	$(\lambda = 3e-1)$		$(\lambda = 2e-2, \lambda_{TV} = 4e-2)$		$(\lambda = 9e-2)$		$(\lambda = 2e-2, \lambda_{TV} = 3e-2)$		$(\lambda = 4e-2)$		$(\lambda = 8e-2, \lambda_{TV} = 2e-2)$	
SNR=30dB	11.1447	0.9742	16.3336	0.9968	17.6827	0.9995	24.0401	0.9994	19.4785	1	26.3681	1
	$(\lambda = 3e-2)$		$(\lambda = 3e-3, \lambda_{TV} = 4e-3)$		$(\lambda = 7e-3)$		$(\lambda = 5e-3, \lambda_{TV} = 5e-3)$		$(\lambda = 5e-3)$		$(\lambda = 3e-2, \lambda_{TV} = 5e-3)$	

of the estimated abundance, and the latter introduces both spectral and spatial weights to exploit the spatial correlation and promote row sparsity. Moreover, DRSU-TV algorithm achieves suboptimal results in all cases due to the simultaneous execution of spectral reweighting and TV regularization, which proves that the multiple constraint strategy can effectively improve the unmixing accuracy. Overall, RDSRSU outperforms comparison algorithms by a substantial degree, indicating that the spatial

weighted factor and TV spatial regularizer mutually improve the unmixing accuracy.

In order to illustrate the advantages of the proposed RDSRSU algorithm in endmember identification based on the spectral library, we take DC1 and DC2 with SNR=20 dB as examples for visual interpretation. Figs. 5 and 6 exhibit the actual abundances and the results obtained by performing the comparison and the proposed unmixing algorithms. For additional clarity, we only show 500 pixels randomly selected from the results. A colored

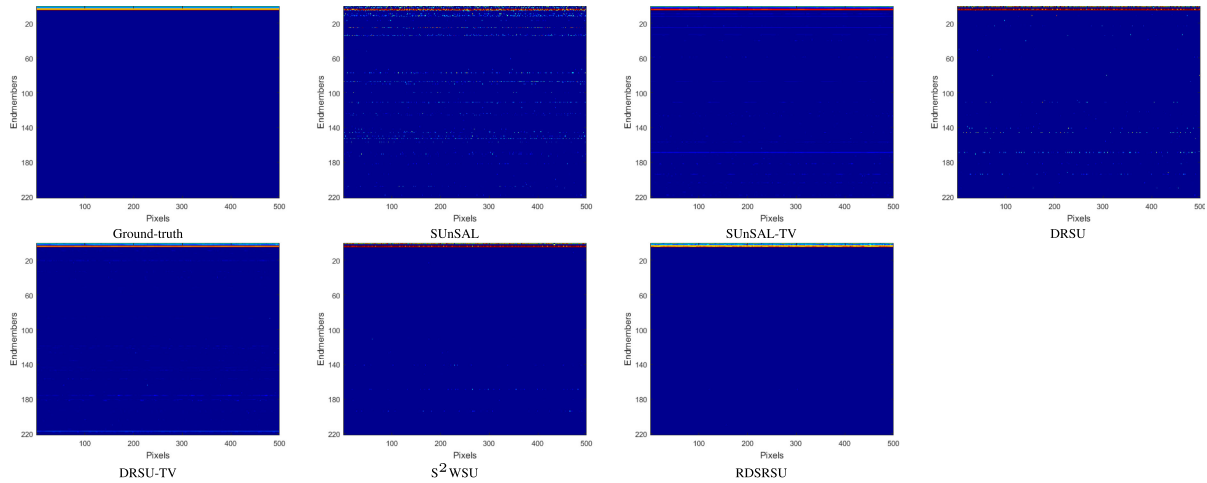


Fig. 5. Actual abundance and estimated abundances obtained by performing comparison algorithms and the proposed RDSRSU algorithm on DC1 when SNR=20 dB.

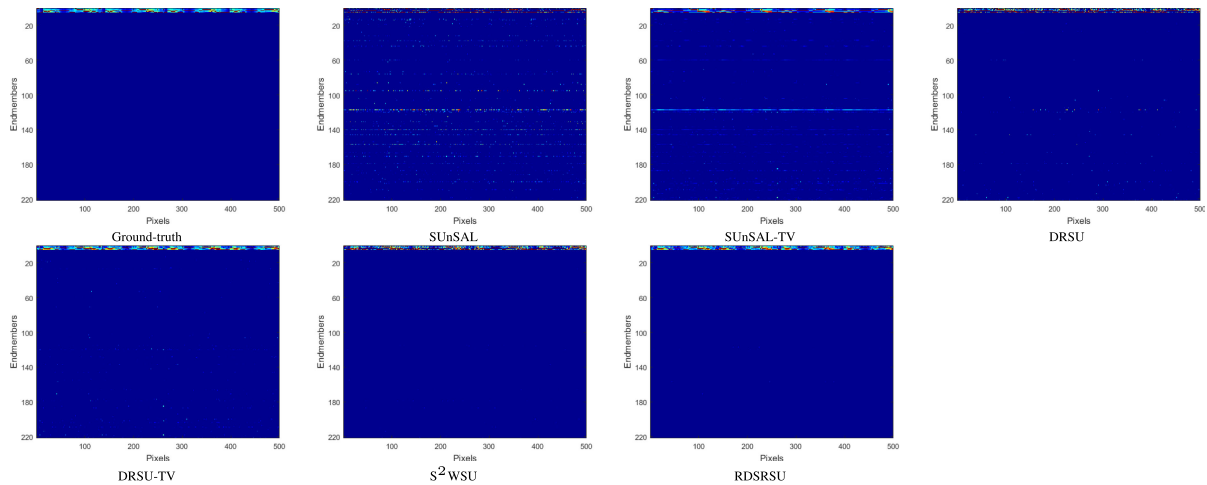


Fig. 6. Actual abundance and estimated abundances obtained by performing comparison algorithms and the proposed RDSRSU algorithm on DC2 when SNR=20 dB.

line in the figure represents the proportion of an endmember. It can be seen from Figs. 5 and 6 that the estimated abundance maps of our method have the best visual effect with few false lines. The colored lines in these two figures are pretty close to the lines in the actual abundance maps in quantity and location. Many noise and false lines present in the results obtained by the SUnSAL and SUnSAL-TV algorithms. There are obviously some outliers and false lines in the results of DRSU and DRSU-TV. The fractional abundance value obtained by S^2 WSU is quite different from the real fractional abundance value. It is demonstrated that the RDSRSU algorithm has strong antinoise performance and can accurately identify endmembers from the spectral library.

To further demonstrate the effectiveness of the proposed RDSRSU method, the abundance maps of endmember 5 obtained by performing different unmixing algorithms on DC1 and DC2 with SNR=20 dB present in Figs. 7 and 8, respectively. For

intuitive comparison, we calculated the differences between the actual abundance and estimated abundances. It can be seen from the Figs. 7 and 8 that the abundance maps estimated by our method are the closest to the actual abundance maps. Compared with the SUnSAL and DRSU algorithms, the abundance maps estimated by the RDSRSU and DRSU-TV algorithms contain less noise. The abundance estimated by SUnSAL-TV is distorted in the transition area and spatial structure details. The S^2 WSU algorithm shows a general abundance estimation effect in these two scene data. As can be seen from the Fig. 7(d), (f) and Fig. 8(d), (f), compared with the DRSU-TV algorithm, the results obtained by the proposed RDSRSU algorithm retain the finer structure and texture information of the image. This further proves that the joint spatial weight and TV regularizer are not susceptible to noise and can improve the unmixing performance.

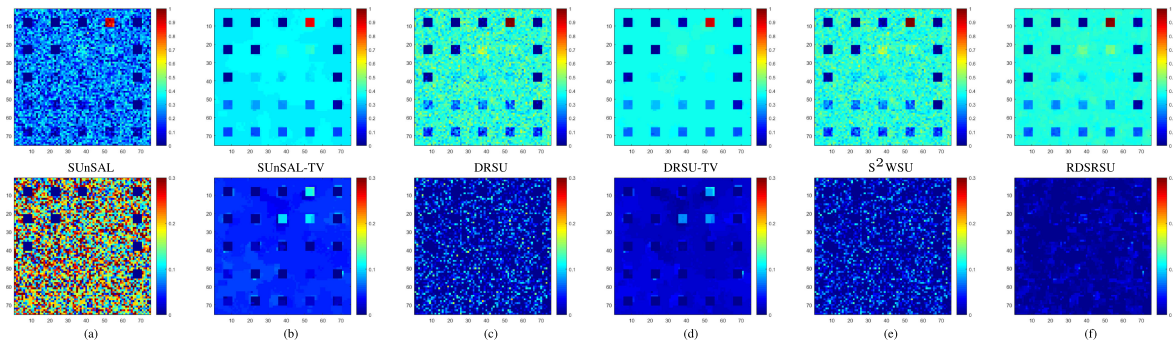


Fig. 7. Fractional abundances of Endmember 5 obtained by performing comparison algorithms and the proposed RDRSRU algorithm on DC1 when SNR=20 dB. Differences between the actual abundance and estimated abundances of Endmember 5. (a) SUnSAL. (b) SUnSAL-TV. (c) DRSU. (d) DRSU-TV. (e) S^2 WSU. (f) RDRSRU.

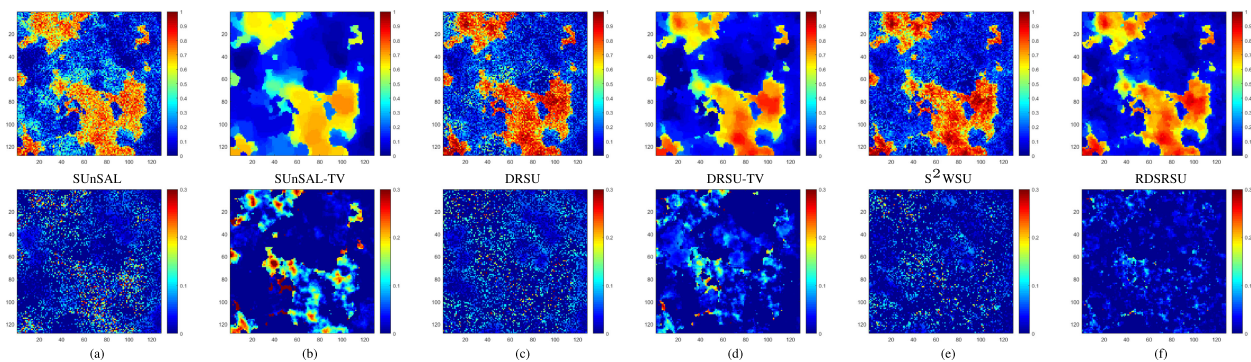


Fig. 8. Fractional abundances of Endmember 5 obtained by performing comparison algorithms and the proposed RDRSRU algorithm on DC2 when SNR=20 dB. Differences between the actual abundance and estimated abundances of Endmember 5. (a) SUnSAL. (b) SUnSAL-TV. (c) DRSU. (d) DRSU-TV. (e) S^2 WSU. (f) RDRSRU.

TABLE III
RUN TIMES (IN SECONDS) OF DIFFERENT UNMIXING METHODS ON PROCESSING DC1 WHEN SNR=20 dB

Algorithm	SUnSAL	SUnSAL-TV	DRSU	DRSU-TV	S^2 WSU	RDRSRU
Time(s)	10.84	115.31	31.56	124.45	45.11	127.55

Table III reports the time consumption of different unmixing methods on processing DC1 when SNR=20 dB. All tests are executed using MATLAB R2016a on a desktop computer with 3.6 GHz Intel Core i7 CPU and 32 GB RAM memory. Note that the time of superpixel segmentation and spatial weight calculation is not reckoned in the time of RDRSRU, since these two steps are processed in advance, and the resulting weights are introduced as constants and will not be recalculated or updated during the unmixing process. From Table III, we can see that SUnSAL takes the shortest time, while other methods are slower because they are derived from SUnSAL. The three methods with TV regularization spend almost the same time and are higher than other methods due to the large computational cost of solving TV term.

In addition, according to [31]–[33], the number of desired superpixel blocks s , as a parameter of SLIC, is vital to the result of superpixel segmentation. In the abovementioned experiments, when SNR=10, 20, and 30 dB, s is set to 2, 2, 6 for DC1,

and 6, 30, 63 for DC2, respectively. To further analyze the impact of superpixel segmentation on the performance of the proposed RDRSRU method, Fig. 9 shows SRE (dB) obtained by RDRSRU on DC1 in the case of different numbers of superpixel blocks. When the noise level is high, dividing the hyperspectral image into fewer superpixel blocks improves the accuracy of the proposed algorithm. For scenes with few pixels, such as DC1 with 75×75 pixels, the image is even suitable to be divided into 2 partitions in the case of low SNR. With the increase of SNR, the proper number of blocks for superpixel segmentation increases, and the effect of segmentation results on the performance of the algorithm decreases. This conclusion indirectly verifies the role of superpixel segmentation in the RDRSRU method. To reduce the negative impact of noise, it is necessary to average a larger superpixel block when the image is heavily contaminated by noise. When the noise level drops,

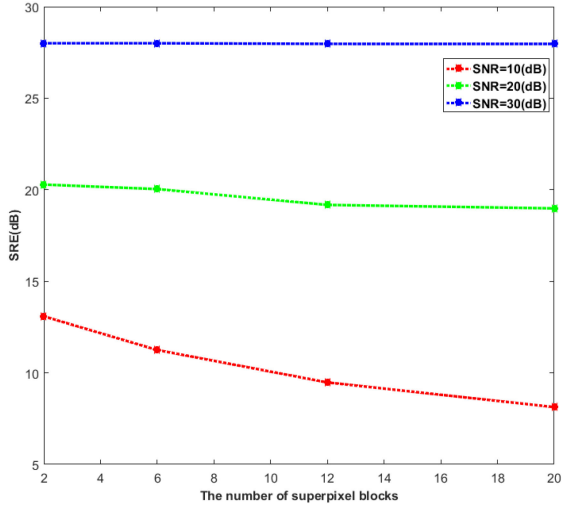


Fig. 9. SRE (dB) obtained by performing the proposed RDSRSU algorithm on DC1 in the case of different numbers of superpixel blocks.

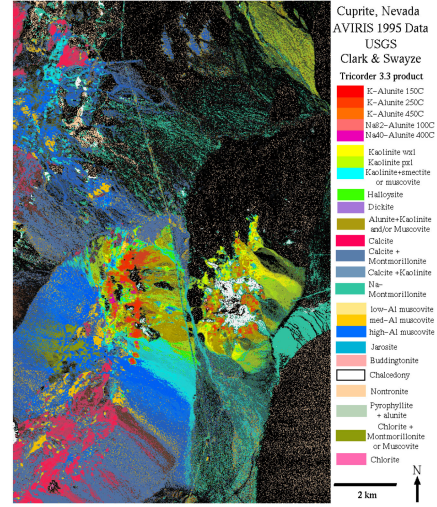


Fig. 10. USGS mineral map of Cuprite mining district in Nevada.

the requirements for denoising are reduced, so the influence of superpixel segmentation is reduced.

V. EXPERIMENTS WITH REAL DATA

In this section, we describe experiments with real data where the proposed RDSRSU algorithm and comparison algorithms were applied to Cuprite dataset and the mangrove dataset, respectively.

A. Cuprite Data

The benchmark Cuprite scene³ consists of 224 bands over the interval from 0.4 to 2.5 μm . The Cuprite data used in the experiment contains 188 bands after removing bands 1-2, 105-115, 150-170, and 223-224 (the low SNR and strong water absorption bands), with the size of 350×350 pixels. The library $A_1 \in \mathbb{R}^{188 \times 240}$ used in this test is the same as that in the DC1 experiment, but the interference bands are removed. Since the actual abundance maps of this data are difficult to obtain, we take the mineral classification map (as shown in Fig. 10⁴) generated by the Tricorder 3.3 software product⁵ [41] as a qualitative reference to evaluate the unmixing performance of each unmixing algorithm.

Three dominant minerals, Alunite, Buddingtonite, and Chalcedony, are chosen as the representatives of the Cuprite area. The optimal settings of the parameters of different unmixing algorithms follow the proposal in the article [30]. For the proposed RDSRSU algorithm, the regularization parameters are set to $(\lambda = 5e-3, \lambda_{TV} = 1e-2)$. For precalculating the spatial weight, the parameter of SLIC is set to $s = 304$, the parameter of SUNSAL is set to $\lambda = 5e-3$. Fig. 11 shows that all algorithms interpret the Cuprite data well, and the abundance maps of these three

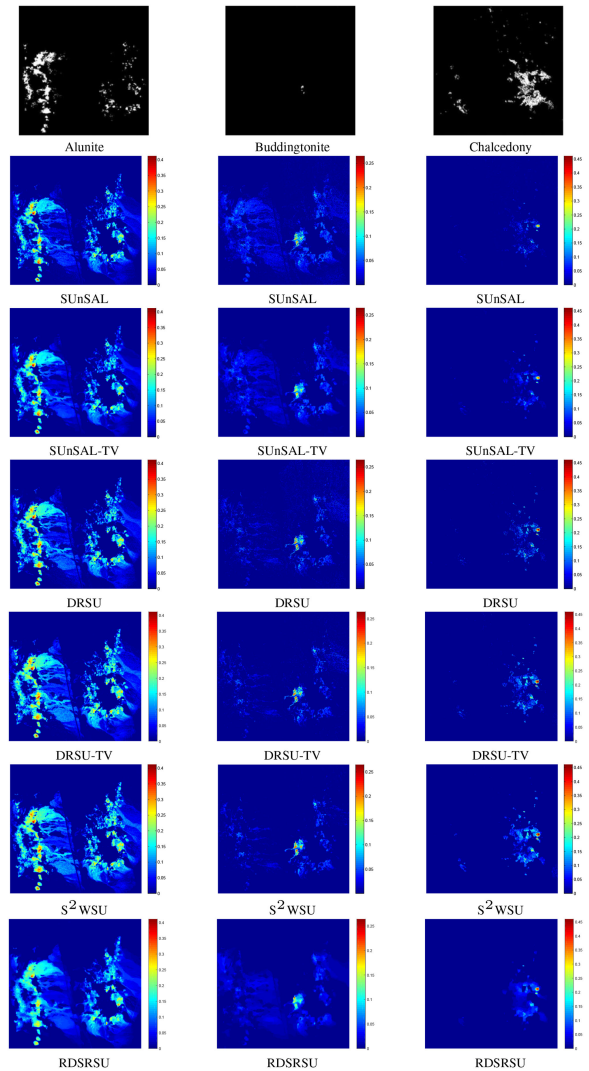


Fig. 11. Abundance maps of three representative minerals obtained by performing comparison algorithms and the proposed RDSRSU algorithm on Cuprite data.

³[Online]. Available: <http://aviris.jpl.nasa.gov/html/aviris.freedata.html>

⁴[Online]. Available: http://speclab.cr.usgs.gov/cuprite95.tgif.2.2um_map.gif

⁵[Online]. Available: <http://speclab.cr.usgs.gov/PAPER/tetracorder>

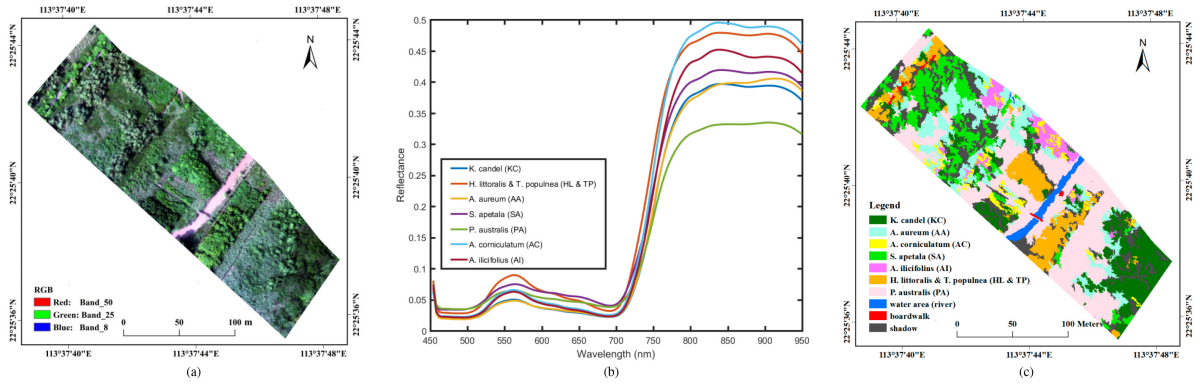


Fig. 12. Mangrove hyperspectral data. (a) UHD185 hyperspectral image. (b) Spectral reflectance profiles of seven vegetation species. (c) Classification map of UHD185 hyperspectral image.

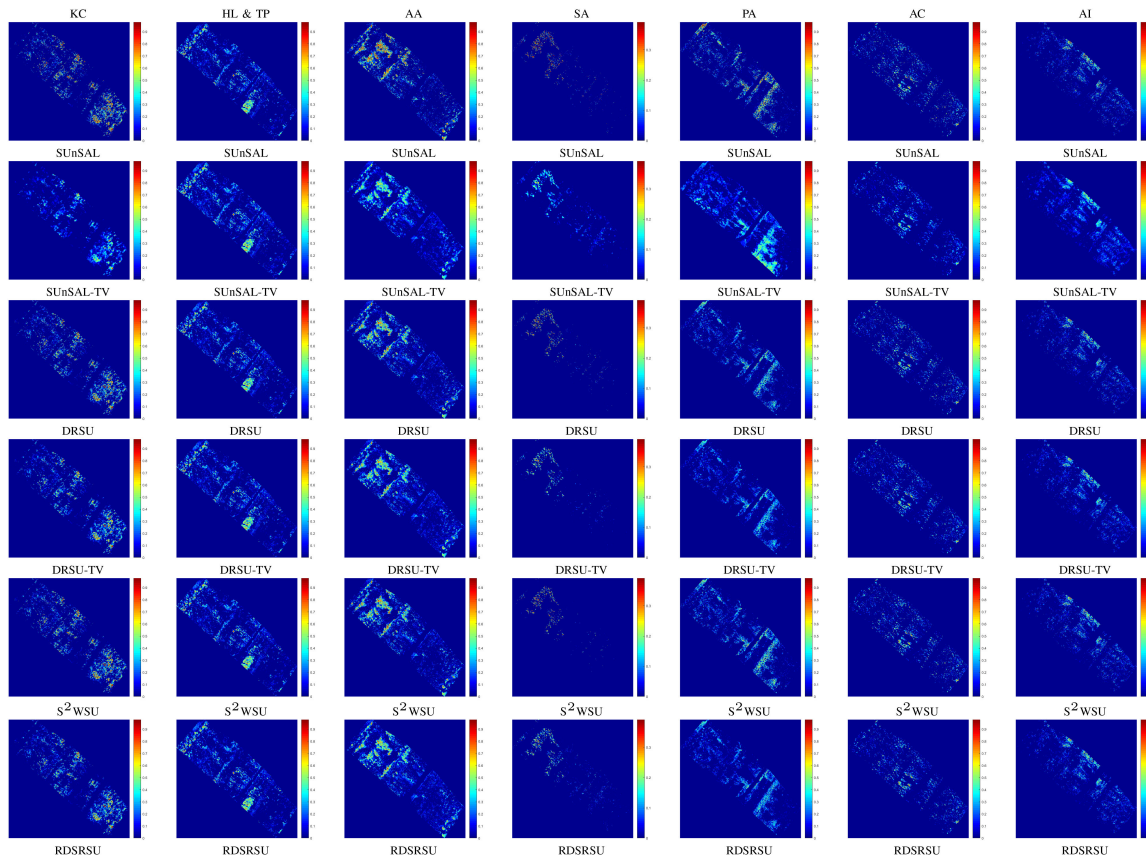


Fig. 13. Abundance maps of seven representative vegetations obtained by performing different sparse unmixing algorithms on mangrove data.

minerals are similar to the reference maps, which proves the effectiveness of the sparse unmixing methods for real datasets. Nevertheless, some subtle differences can still be found from the abundance maps estimated by each algorithm. The abundance map (e.g., Buddingtonite) estimated by the SUnSAL algorithm looks noisy, while the result obtained by SUnSAL-TV is obviously oversmooth. The results estimated by DRSU algorithm do not show good spatial consistency (e.g., Chalcodony mineral). The results obtained by the RDSRSU, DRSU-TV, and S^2 WSU

algorithms are almost the same as the reference. However, the proposed RDSRSU algorithm shows better performance for Alunite and suppresses the oversmoothing phenomenon to a certain extent. Therefore, we can conclude that the newly proposed RDSRSU algorithm can effectively interpret the real data.

B. Mangrove Data

The mangrove dataset was collected by Cubert UHD185 hyperspectral imaging system onboard the unmanned aerial vehicle (UAV) platform in 2016, covering part of Qi'ao Island Mangrove Nature Reserve, Zhuhai City, Guangdong Province, China. This area is one of the places with the most species of mangrove plants in China. The size of the study scene is 1878×1877 pixels with 125 spectral bands covering the wavelength range from 450 to 950 nm, as shown in Fig. 12(a) [42]. According to [42] and [43], the mangrove species distributed in the study area mainly include *K. candel* (KC), *S. apetala* (SA), *H. littoralis* (HL) and *T. populnea* (TP), *A. aureum* (AA), *A. corniculatum* (AC), and *A. ilicifolius* (AI). In addition, it also includes *P. australis* (PA), water area (river), and boardwalks. Affected by the lighting conditions, there are some shadows in the UAV hyperspectral image, which are also considered to be distinct endmembers in the experimental.

There is no available spectral library for this data, which is essential for the sparse unmixing algorithm. Therefore, we specially build a spectral library for the mangrove hyperspectral data in this article. First, we determine the homogeneous region where each type of ground object is located in the UAV hyperspectral image following field investigation. Each homogeneous region can be approximately considered as a pure pixel region, and then the average value of this region is calculated as the spectral signature of the corresponding ground object. Finally, the spectral library $\mathbf{A}_3 \in \mathbb{R}^{125 \times 23}$ is built, which contains the spectral signatures of mangrove species, PA, river, boardwalks and shadows. Fig. 12(b) shows the reflectance spectrum curves of seven typical types of vegetation in the library \mathbf{A}_3 . It can be seen that the various vegetation curves are relatively close, which brings challenges to the unmixing task. This experiment takes the mangrove species classification map of the study area obtained by the support vector machine method in [42] as the reference data [as shown in Fig. 12(c)] to analyze the unmixing performance of each algorithm qualitatively.

In this experiment, the regularization parameters of SUNSAL, DRSU, and S^2 WSU were empirically set to $\lambda = 1e-4$, $\lambda = 8e-5$, and $\lambda = 1e-4$, respectively, whereas the parameters for SUnSAL-TV, DRSU-TV, and RDSRSU were set to ($\lambda = 1e-3, \lambda_{TV} = 1e-3$), ($\lambda = 6e-5, \lambda_{TV} = 6e-5$), and ($\lambda = 1e-3, \lambda_{TV} = 1e-6$), respectively. In the process of precalculating the spatial weight for RDSRSU, the parameter of SLIC is set to $s = 592$, the parameter of SUnSAL is set to $\lambda = 1e-6$. Fig. 13 shows the abundance map of each typical vegetation estimated by different unmixing algorithms, including KC, HL and TP, AA, SA, PA, AC, and AI. The position in the image whose value is greater than zero indicates that the vegetation is distributed here. Fig. 13 shows that the abundance maps of all six unmixing algorithms are close to the reference classification map, which proves that the sparse unmixing algorithm can effectively unmix mangrove hyperspectral data. Although it is difficult to quantitatively evaluate the unmixing results of each algorithm, it can be qualitatively observed from Fig. 13 that the proposed

RDSRSU algorithm achieved approximately consistent results with the reference classification map. As shown in Fig. 12(b), the spectral curves of seven vegetation species are highly similar, which makes it difficult for the sparse unmixing algorithm to accurately find the actual endmembers from the spectral library. Even so, the abundance maps of each endmember obtained by the RDSRSU algorithm clearly reflect the distribution of various types of vegetation and retain fine spatial details, which illustrates the advantage of our method in unmixing mangrove data.

VI. CONCLUSION AND FUTURE WORK

In this article, we have developed a novel double spatial regularization method for robust sparse hyperspectral unmixing. The proposed RDSRSU model depicts the spatial information of the image from the perspective of spatial weighting constraints and TV regularization to achieve precise extraction of spatial information. The experiments with synthetic and real hyperspectral data show that joint double spatial regularization strategy is conducive to valid endmember identification based on the spectral library, thereby obtaining stable and accurate unmixing results. It draws inspiration for spatial regularized sparse unmixing, especially for unmixing hyperspectral images contaminated by high noise. In future work, we will take deep networks [44], [45] on sparse hyperspectral unmixing and explore automatic processing for hyperspectral data interpretation [46], [47].

REFERENCES

- [1] N. Keshava and J. F. Mustard, "Spectral unmixing," *IEEE Signal Process. Mag.*, vol. 19, no. 1, pp. 44–57, Jan. 2002.
- [2] J. M. Bioucas-Dias *et al.*, "Hyperspectral unmixing overview: Geometrical, statistical, and sparse regression-based approaches," *IEEE J. Sel. Topics Appl. Earth Observ. Remote Sens.*, vol. 5, no. 2, pp. 354–379, Apr. 2012.
- [3] J. Boardman, F. Kruse, and R. Green, "Mapping target signatures via partial unmixing of AVIRIS data," in *Proc. JPL Airborne Earth Sci. Workshop*, 1995, pp. 23–26.
- [4] M. E. Winter, "N-FINDR: An algorithm for fast autonomous spectral end-member determination in hyperspectral data," *Proc. SPIE Imag. Spectrometry V*, vol. 3753, pp. 266–275, 1999.
- [5] J. M. Nascimento and J. M. Bioucas-Dias, "Vertex component analysis: A fast algorithm to unmix hyperspectral data," *IEEE Trans. Geosci. Remote Sens.*, vol. 43, no. 4, pp. 898–910, Apr. 2005.
- [6] J. Li, A. Agathos, D. Zaharie, J. M. Bioucas-Dias, A. Plaza, and X. Li, "Minimum volume simplex analysis: A fast algorithm for linear hyperspectral unmixing," *IEEE Trans. Geosci. Remote Sens.*, vol. 53, no. 9, pp. 5067–5082, Sep. 2015.
- [7] S. Zhang, A. Agathos, and J. Li, "Robust minimum volume simplex analysis for hyperspectral unmixing," *IEEE Trans. Geosci. Remote Sens.*, vol. 55, no. 11, pp. 6431–6439, Nov. 2017.
- [8] M. Berman, H. Kiiveri, R. Lagerstrom, A. Ernst, R. Dunne, and J. F. Huntington, "ICE: A statistical approach to identifying endmembers in hyperspectral images," *IEEE Trans. Geosci. Remote Sens.*, vol. 42, no. 10, pp. 2085–2095, Oct. 2004.
- [9] J. M. Nascimento and J. M. Bioucas-Dias, "Does independent component analysis play a role in unmixing hyperspectral data?," *IEEE Trans. Geosci. Remote Sens.*, vol. 43, no. 1, pp. 175–187, Jan. 2005.
- [10] M.-D. Iordache, J. M. Bioucas-Dias, and A. Plaza, "Sparse unmixing of hyperspectral data," *IEEE Trans. Geosci. Remote Sens.*, vol. 49, no. 6, pp. 2014–2039, Jun. 2011.
- [11] L. Qi, J. Li, Y. Wang, Y. Huang, and X. Gao, "Spectral-spatial-weighted multiview collaborative sparse unmixing for hyperspectral images," *IEEE Trans. Geosci. Remote Sens.*, vol. 58, no. 12, pp. 8766–8779, Dec. 2020.

- [12] F. Li, S. Zhang, B. Liang, C. Deng, C. Xu, and S. Wang, "Hyperspectral sparse unmixing with spectral-spatial low-rank constraint," *IEEE J. Sel. Topics Appl. Earth Observ. Remote Sens.*, vol. 14, pp. 6119–6130, Jun. 2021.
- [13] M.-D. Iordache, J. M. Bioucas-Dias, and A. Plaza, "Collaborative sparse regression for hyperspectral unmixing," *IEEE Trans. Geosci. Remote Sens.*, vol. 52, no. 1, pp. 341–354, Jan. 2014.
- [14] F. Chen and Y. Zhang, "Sparse hyperspectral unmixing based on constrained $l_p - l_2$ optimization," *IEEE Geosci. Remote Sens. Lett.*, vol. 10, no. 5, pp. 1142–1146, Sep. 2013.
- [15] E. J. Candès, M. B. Wakin, and S. P. Boyd, "Enhancing sparsity by reweighted l_1 minimization," *J. Fourier Anal. Appl.*, vol. 14, no. 5, pp. 877–905, 2008.
- [16] C. Y. Zheng, H. Li, Q. Wang, and C. L. Philip Chen, "Reweighted sparse regression for hyperspectral unmixing," *IEEE Trans. Geosci. Remote Sens.*, vol. 54, no. 1, pp. 479–488, Jan. 2016.
- [17] R. Wang, H. C. Li, W. Liao, and A. Piñurica, "Double reweighted sparse regression for hyperspectral unmixing," in *Proc. IEEE Int. Geosci. Remote Sens. Symp.*, 2016, pp. 6986–6989.
- [18] C. Shi and L. Wang, "Incorporating spatial information in spectral unmixing: A review," *Remote Sens. Environ.*, vol. 149, pp. 70–87, 2014.
- [19] M.-D. Iordache, J. M. Bioucas-Dias, and A. Plaza, "Total variation spatial regularization for sparse hyperspectral unmixing," *IEEE Trans. Geosci. Remote Sens.*, vol. 50, no. 11, pp. 4484–4502, Nov. 2012.
- [20] R. Wang, H. C. Li, A. Pizurica, J. Li, A. Plaza, and W. J. Emery, "Hyperspectral unmixing using double reweighted sparse regression and total variation," *IEEE Geosci. Remote Sens. Lett.*, vol. 14, no. 7, pp. 1146–1150, Jul. 2017.
- [21] Y. Zhong, R. Feng, and L. Zhang, "Non-local sparse unmixing for hyperspectral remote sensing imagery," *IEEE J. Sel. Topics Appl. Earth Observ. Remote Sens.*, vol. 7, no. 6, pp. 1889–1909, Jun. 2014.
- [22] R. Wang, H-C Li, W. Liao, X. Huang, and W. Philips, "Centralized collaborative sparse unmixing for hyperspectral images," *IEEE J. Sel. Topics Appl. Earth Observ. Remote Sens.*, vol. 10, no. 5, pp. 1949–1962, May 2017.
- [23] J. Li, Y. Li, R. Song, S. Mei, and Q. Du, "Local spectral similarity preserving regularized robust sparse hyperspectral unmixing," *IEEE Trans. Geosci. Remote Sens.*, vol. 57, no. 10, pp. 7756–7769, Oct. 2019.
- [24] B. Tu, J. Wang, X. Kang, G. Zhang, X. Ou, and L. Guo, "KNN-based representation of superpixels for hyperspectral image classification," *IEEE J. Sel. Topics Appl. Earth Observ. Remote Sens.*, vol. 11, no. 11, pp. 4032–4047, Nov. 2018.
- [25] S. Zhang *et al.*, "Superpixel-guided sparse unmixing for remotely sensed hyperspectral imagery," in *Proc. IEEE Int. Geosci. Remote Sens. Symp.*, 2019, pp. 2155–2158.
- [26] C. Liu, J. Li, and L. He, "Superpixel-based semisupervised active learning for hyperspectral image classification," *IEEE J. Sel. Topics Appl. Earth Observ. Remote Sens.*, vol. 12, no. 1, pp. 357–370, Jan. 2019.
- [27] R. A. Borsoi, T. Imbiriba, C. M. JoséBermudez, and C. Richard, "A fast multiscale spatial regularization for sparse hyperspectral unmixing," *IEEE Geosci. Remote Sens. Lett.*, vol. 16, no. 4, pp. 598–602, Apr. 2019.
- [28] H. Li, R. Feng, L. Wang, Y. Zhong, and L. Zhang, "Superpixel-based reweighted low-rank and total variation sparse unmixing for hyperspectral remote sensing imagery," *IEEE Trans. Geosci. Remote Sens.*, vol. 59, no. 1, pp. 629–647, Jan. 2021.
- [29] B. Tu, S. Huang, L. Fang, G. Zhang, J. Wang, and B. Zheng, "Hyperspectral image classification via weighted joint nearest neighbor and sparse representation," *IEEE J. Sel. Topics Appl. Earth Observ. Remote Sens.*, vol. 11, no. 11, pp. 4063–4075, Nov. 2018.
- [30] S. Zhang, J. Li, H. Li, C. Deng, and A. Plaza, "Spectral-spatial weighted sparse regression for hyperspectral image unmixing," *IEEE Trans. Geosci. Remote Sens.*, vol. 56, no. 6, pp. 3265–3276, Jun. 2018.
- [31] R. Achanta, A. Shaji, K. Smith, A. Lucchi, P. Fua, and S. Süsstrunk, "SLIC superpixels compared to state-of-the-art superpixel methods," *IEEE Trans. Pattern Anal. Mach. Intell.*, vol. 34, no. 11, pp. 2274–2282, Nov. 2012.
- [32] X. Xu, J. Li, C. Wu, and A. Plaza, "Regional clustering-based spatial preprocessing for hyperspectral unmixing," *Remote Sens. Environ.*, vol. 204, pp. 333–346, 2018.
- [33] X. Wang, Y. Zhong, L. Zhang, and Y. Xu, "Spatial group sparsity regularized nonnegative matrix factorization for hyperspectral unmixing," *IEEE Trans. Geosci. Remote Sens.*, vol. 55, no. 11, pp. 6287–6304, Nov. 2017.
- [34] Z. Wu, W. Zhu, J. Chanussot, Y. Xu, and S. Osher, "Hyperspectral anomaly detection via global and local joint modeling of background," *IEEE Trans. Signal Process.*, vol. 67, no. 14, pp. 3858–3869, Jul. 2019.
- [35] X. Xu, B. Pan, Z. Chen, Z. Shi, and T. Li, "Simultaneously multiobjective sparse unmixing and library pruning for hyperspectral imagery," *IEEE Trans. Geosci. Remote Sens.*, vol. 59, no. 4, pp. 3383–3395, Apr. 2021.
- [36] T. Ince, "Double spatial graph Laplacian regularization for sparse unmixing," *IEEE Geosci. Remote Sens. Lett.*, to be published, doi: 10.1109/LGRS.2021.3065989.
- [37] T. Ince, "Superpixel-based graph Laplacian regularization for sparse hyperspectral unmixing," *IEEE Geosci. Remote Sens. Lett.*, to be published, doi: 10.1109/LGRS.2020.3027055.
- [38] P. V. Giampouras, K. E. Themelis, A. A. Rontogiannis, and K. D. Koutroumbas, "Simultaneously sparse and low-rank abundance matrix estimation for hyperspectral image unmixing," *IEEE Trans. Geosci. Remote Sens.*, vol. 54, no. 8, pp. 4775–4789, Aug. 2016.
- [39] J. Huang, T. Huang, L. Deng, and X. Zhao, "Joint-sparse-blocks and low-rank representation for hyperspectral unmixing," *IEEE Trans. Geosci. Remote Sens.*, vol. 57, no. 4, pp. 2419–2438, Apr. 2019.
- [40] J. M. Bioucas-Dias and M. Figueiredo, "Alternating direction algorithms for constrained sparse regression: Application to hyperspectral unmixing," in *Proc. 2nd Workshop Hyperspectr. Image Signal Process.-Evol. Remote Sens.*, 2010, pp. 1–4.
- [41] R. Clark *et al.*, "Imaging spectroscopy: Earth and planetary remote sensing with the USGS tetra-corder and expert systems," *J. Geophys. Res.*, vol. 108, no. E12, pp. 5131–5135, Dec. 2003.
- [42] J. Cao, W. Leng, K. Liu, L. Liu, Z. He, and Y. Zhu, "Object-based mangrove species classification using unmanned aerial vehicle hyperspectral images and digital surface models," *Remote Sens.*, vol. 10, no. 1, p. 89, 2018.
- [43] J. Cao, K. Liu, L. Liu, Y. Zhu, J. Li, and Z. He, "Identifying mangrove species using field close-range snapshot hyperspectral imaging and machine-learning techniques," *Remote Sens.*, vol. 10, no. 12, 2018, Art. no. 2047.
- [44] J. Li *et al.*, "Deep hybrid 2-D-3-D CNN based on dual second-order attention with camera spectral sensitivity prior for spectral super-resolution," *IEEE Trans. Neural Netw. Learn. Syst.*, to be published, doi: 10.1109/TNNLS.2021.3098767.
- [45] Y. Su, J. Li, A. Plaza, A. Marinoni, P. Gamba, and S. Chakravorty, "DAEN: Deep autoencoder networks for hyperspectral unmixing," *IEEE Trans. Geosci. Remote Sens.*, vol. 57, no. 7, pp. 4309–4321, Jul. 2019.
- [46] Z. Wu *et al.*, "Scheduling-guided automatic processing of massive hyperspectral image classification on cloud computing architectures," *IEEE Trans. Cybern.*, vol. 51, no. 7, pp. 3588–3601, Jul. 2021.
- [47] Z. Wu, J. Sun, Y. Zhang, Z. Wei, and J. Chanussot, "Recent developments in parallel and distributed computing for remotely sensed Big Data processing," *Proc. IEEE*, vol. 109, no. 8, pp. 1282–1305, Aug. 2021.



Fan Li received the B.S. degree in computer science and technology from Wuhan University, Wuhan, China, in 2004, and the M.E. degree in computer technology from Jiangxi Normal University, Nanchang, China, in 2020.

She is currently a Lecturer with the School of Information Engineering, Nanchang Institute of Technology, Nanchang, China. Her research interests include hyperspectral unmixing and low-rank representation.



Shaquan Zhang (Member, IEEE) received the B.S. degree in communication engineering and the M.E. degree in power engineering from the Nanchang Institute of Technology, Nanchang, China, in 2012 and 2015, respectively, and the Ph.D. degree in cartography and geography information system from Sun Yat-sen University, Guangzhou, China, in 2018.

He is currently an Associate Professor with the School of Information Engineering, Nanchang Institute of Technology, Nanchang, China. His research interests include hyperspectral unmixing, sparse representation, and machine learning.



Chengzhi Deng received the B.S. degree in communication engineering and the M.S. degree in optics from Jiangxi Normal University, Nanchang, China, in 2002 and 2005, respectively, and the Ph.D. degree in information and communication engineering from the Huazhong University of Science and Technology, Wuhan, China, in 2008.

He is currently a Professor with the School of Information Engineering, Nanchang Institute of Technology, Nanchang, China. He is also the Deputy Director of Jiangxi Province Key Laboratory of Water Information Cooperative Sensing and Intelligent Processing. His research interests include hyperspectral image processing, machine learning, and remote sensing of water environment.



Jingjing Cao received the B.S. degree in geographic information system from Xinyang Normal University, Xinyang, China, in 2011, and the M.S. and Ph.D. degrees in cartography and geographic information system from Sun Yat-sen University, Guangzhou, China, in 2013 and 2019, respectively.

She is currently a Postdoctoral Researcher with the School of Geography and Planning, Sun Yat-sen University, Guangzhou, China. Her current research interests include vegetation remote sensing and urban remote sensing, concentrating on mangrove species classification, hyperspectral image analysis, unmanned aerial vehicle remote sensing, machine learning, and spatio-temporal data information mining.



Bingkun Liang received the B.S. degree in civil engineering from Hunan Agricultural University, Changsha, China, in 2016, and the M.S. degree in ethnology in 2019 from Sun Yat-sen University, Guangzhou, China, where he is currently working toward the Ph.D. degree in cartography and geography information system with the School of Geography and Planning.

His major research interests include spectral unmixing, signal processing, and remote sensing.



Shengqian Wang received the M.S. degree in theoretical physics from Jiangxi Normal University, Nanchang, China, in 1995, and the Ph.D. degree in information and communication engineering from Shanghai Jiao Tong University, Shanghai, China, in 2002.

He is currently a Professor with the School of Information Engineering, Nanchang Institute of Technology, Nanchang, China. He is also the Director of Jiangxi Province Key Laboratory of Water Information Cooperative Sensing and Intelligent Processing. His research interests include hyperspectral image processing, machine learning, and hydrological information processing.